Radiation Physics and Chemistry 236 (2025) 112890

Contents lists available at ScienceDirect

Radiation Physics and Chemistry

journal homepage: www.elsevier.com/locate/radphyschem

Opto-physical, microstructural, X-ray and gamma-ray attenuation efficiency of ore-driven SiO_2 and Bi_2O_3 glasses reinforced with BaO

Abubakar Sadiq Aliyu [a,b,*], Sulaiman Yaro Jibrin [a], Amina Muhammad Dunama [a,b], Umar Sa'ad Aliyu [a,b], Abdulkarim Muhammad Hamza [a,b], Bemgba Bevan Nyakuma [c], Jamilu Ari Labaran [b], Yahaya Musa [d], Abdulsamad Asuku [d], Sani Muhammad [a]

[a] Muhammadu Buhari TETFund Centre for Excellence, Federal University of Lafia, P. M. B 146, Lafia, Nasarawa State, Nigeria
[b] Department of Physics, Faculty of Sciences, Federal University of Lafia, P. M. B 146, Lafia, Nasarawa State, Nigeria
[c] Department of Chemical Sciences, Faculty of Science and Computing, North-Eastern University, P. M. B. 0198, Gombe, Gombe State, Nigeria
[d] Nuclear Science and Technology Section, Centre for Energy Research and Training, Ahmadu Bello University, Zaria, Nigeria

ARTICLE INFO

Handling Editor: Dr. Chris Chantler

Keywords:
Quartz
Glass
Shielding glass
X-ray attenuation
Gamma rays
Radiation shielding

ABSTRACT

The development of cost-effective and sustainable radiation-attenuating materials is crucial for enhancing radiation safety in various applications. This study reports the development of novel transparent X and gamma-ray attenuating glass systems using glass sand and bismuth oxide, with an empirical formula of $\{85[25\ (Quartz) + 35H_3BO_3 + 40Na_2CO_3] + 15BaO\}_{(100-y)} + [Bismuth\ ore]_y$. The glasses were characterized using XRF, EDX, XRD, FTIR, and physical density measurements, revealing improved opto-physical and radiation shielding properties. The Bi ore and quartz contain 60.68 wt% and 89.97 wt% of Bi_2O_3 and SiO_2, respectively. The physical densities of the glasses increased from 2.92 g/cm^3 to 3.53 g/cm^3 with increasing Bi_2O_3 content, indicating improved mass attenuation. XRD analysis confirmed the amorphous nature of the glasses, while FTIR spectroscopy revealed BO_3 and SiO_4 groups. Attenuation experiments with Cs-137 (662 keV) showed that the sample Y25 (25 wt% Bi oxide) has the lowest Tenth Value Layer (TVL) and Mean Free Path (MFP), indicating improved gamma-ray attenuation compared to commercially available Pb/Ba glasses. This study demonstrates the novelty of using locally sourced materials to fabricate radiation-attenuating glasses with potential applications in radiation safety, highlighting its potential for industrial scalability.

1. Introduction

The use of heavy metal oxides in fabricating nuclear shielding glasses to replace lead (Pb) oxide has garnered significant attention among researchers in glass science and technology. Various studies have explored alternative materials, such as $LiBi_5OBEu_2$ glass systems, which exhibit higher gamma and neutron attenuation efficiencies than $LiPb_5OBEu$ glasses (Almisned et al., 2021). Additionally, the incorporation of heavy metal oxides in TBBE glasses has been shown to enhance gamma and neutron attenuation efficiencies compared to conventional materials like graphite, water, and concrete (Al-Buriahi et al., 2021). Furthermore, metal composites comprising sulfated cerium and bismuth oxide have demonstrated 92 % shielding efficiency for 60 keV X-rays, highlighting their potential as flexible substitutes for Pb and other heavy metals-based composites (Mahalingam et al., 2023). Consequently, our research takes a pioneering approach by utilizing locally sourced bismuth ore and glass sand to develop novel radiation-attenuating glasses, thereby introducing a new frontier in sustainable and cost-effective radiation shielding materials.

Furthermore, research has shown that doping polyester samples with 25 wt% of Bi_2O_3 and CdO enhance their radiation shielding efficiency compared to samples containing $PbCO_3$ (Aloraini et al., 2023). Additionally, Subedi & Lamichhane (Subedi and Lamichhane, 2023) demonstrated that low-density Ti-based bulk metallic glass composites exhibit better shielding efficiency for gamma rays, fast neutrons, and H^1/He^{+2} ions than Pb-based materials. Similarly, increasing the wt.% of Bi_2O_3 and coating thickness improves gamma-ray attenuation in Bi_2O_3/epoxy resin-coated composites, while adding 5 wt% tantalum to the composite increases the system's β-ray attenuation efficiency by approximately 3 % (Li et al., 2022). The increase in BaO concentration in

* Corresponding author. Muhammadu Buhari TETFund Centre for Excellence, Federal University of Lafia, P. M. B 146, Lafia, Nasarawa State, Nigeria.
E-mail addresses: abubakar.aliyu@science.fulafia.edu.ng, abubakarsaliyu@nsuk.edu.ng (A.S. Aliyu).

https://doi.org/10.1016/j.radphyschem.2025.112890
Received 8 February 2025; Received in revised form 26 April 2025; Accepted 28 April 2025
Available online 1 May 2025

glasses also enhances their optical and radiation shielding properties, suggesting potential use as a substitute for optoelectronics and shielding applications (Shaaban et al., 2022) (Khazaalah et al., 2022) (Sriwongsa et al., 2023). The current research builds upon these findings by exploring the use of mineral ores, specifically bismuth ore and glass sand, as sustainable and cost-effective alternatives for fabricating radiation-attenuating glasses. This approach has the potential to drive innovation in the field of radiation safety and open up new opportunities for applications in various industries.

BaO-doped glasses outperform Bi_2O_3 and PbO doped glasses in radiation shielding efficiency, particularly when combined with ZnO and B_2O_3, due to BaO's high density and effective atomic number (Aboud et al., 2022). The integration of BaO and Bi_2O_3 in various glass systems significantly improves the radiation shielding, mechanical, and catalytic properties of the glasses. Higher concentrations of Bi_2O_3 enhance the glass systems' mass density and molecular weight, while decreasing elasticity, suggesting a balance between improved attenuation efficiency and mechanical elasticity (Dogra et al., 2018). Additionally, Bi_2O_3-based catalysts and photocatalysts demonstrate excellent performance in environmental applications, while BaO additions enhance the structural and magnetic properties of composite materials (Mohammed and Dachuru, 2024).

Silica is a fundamental component in the glass network that provides structural stability. In certain compositions, a low concentration of SiO_2 may not be enough to form a stable glass network, necessitating the addition of other oxides. (El Din et al., 2024). Silica-based glasses, when combined with heavy metal oxides like bismuth, provide superior gamma-ray shielding properties, making them ideal for radiological applications (Singh et al., 2014).

Bismuth oxide enhances the radiation-shielding properties of glasses by increasing density and mass attenuation coefficient, which significantly improves the ability to attenuate gamma rays and neutrons (Sayyed et al., 2025), (Zaid et al., 2021). The addition of Bi_2O_3 to silicate and borate glasses improves their optical properties and radiation shielding efficiency, making them a promising alternative to lead-based glasses (Zaid et al., 2021), (Alonizan et al., 2023a). The presence of Bi_2O_3 enhances the thermal stability and mechanical robustness of the glass.

Barium oxide (BaO) is frequently combined with other oxides in glasses to enhance radiation shielding properties. It contributes to the density and structural integrity of the glass, enhancing its ability to absorb radiation (Alonizan et al., 2023a). Studies show that replacing BaO with Bi_2O_3 in borate glasses improves gamma-ray shielding properties, suggesting the potential for optimizing glass compositions for specific shielding applications (Ratep et al., 2023).

Boron oxide (B_2O_3) plays a significant role in the formation of a stable glass network and enhances the ability of glass to attenuate neutrons due to its high neutron absorption cross-section (El Din et al., 2024). The incorporation of B_2O_3 in silicate glasses, along with Bi_2O_3, improves the thermal stability and mechanical properties of glass, enhancing nuclear applications (El Din et al., 2024), (Alonizan et al., 2023b). Additionally, B_2O_3 contributes to the optical transparency and UV absorption capabilities of the glass (El Din et al., 2024).

Boric acid (H_3BO_3) significantly influences the physical properties and stability of fabricated glass. It is commonly used in the preparation of alkali borate glasses, where it contributes to the formation of a glass network by bonding with oxygen (Karthika et al., 2025). H_3BO_3 impacts the refractive index and thermal expansion properties of sodium borosilicate glasses, with the refractive index reaching its maximum at specific concentrations (Turner, 1924). Additionally, H_3BO_3 plays a crucial role in the vitrification process of low-activity waste, acting as an early melting glass former and influencing the volatilization behaviour of other salts (Aliyu et al., 2024a), (Aliyu et al., 2024b).

Sodium carbonate (Na_2CO_3) is a crucial component in glass fabrication, used as a flux to reduce the melting temperature of the glass mixture. In the preparation of alkali borate glasses, Na_2CO_3 is used with H_3BO_3 to form sodium borate glasses (Karthika et al., 2025). Na_2CO_3 also plays a role in the electro-melting process of high-alkali borosilicate glass, where it affects the evaporation of sodium and boron oxides, thereby influencing the final glass composition and properties (Sobolev et al., 1987). Furthermore, Na_2CO_3 plays a crucial role in low-activity waste vitrification, influencing the retention and volatilization of other salts during the melting process (Nienhuis and McCloy, 2020).

Despite the growing interest in the benefits of co-doping glass systems with BaO and Bi_2O_3, there is a notable gap in the scientific literature. The research gap exists in utilizing BaO, Bi ore, and glass sand for fabricating highly transparent and radiation-attenuating glass systems required for specialized applications. The current study addresses this gap by investigating the optical, physical, structural, and nuclear radiation attenuation characteristics of novel glasses synthesized from quartz, bismuth ore, and analytical BaO. This research also provides comprehensive data on the elemental composition and morphological structure of silica sand and bismuth ores from northern Nigeria, highlighting their potential for advanced applications. Lastly, the study aims to develop sustainable and high-performance radiation shielding materials by exploring the synergistic effects of BaO and Bi_2O_3-containing ores in glasses.

2. Materials and method

The glass fabrication process utilized the following materials: quartz (glass sand), bismuth ore, and high-purity chemicals including boric acid (H_3BO_3, 99.9 %), barium oxide (BaO, 99.9 %), and sodium carbonate (Na_2CO_3, 99.9 %).

2.1. Samples collection and preparation

Quartz was sourced from Shabu (Lafia North) in Nasarawa State, Nigeria, with geographical coordinates of Latitude 8°34′ N and Longitude 8°33′ E, and an elevation of 342 m. Next, the glass sand was pulverised by grinding and sieving (Fig. 1) before Energy Dispersive X-ray Fluorescence (EDXRF) analysis. Bismuth ore in clayey form was sourced from Falgore forests in Kano State, Nigeria, with GPS coordinates of Latitude 10°43′59″ N and Longitude 8°45′0″ E. The collected Bi ore samples are shown in Fig. 2 (Aliyu et al., 2024a), (Aliyu et al., 2024b).

2.2. Energy Dispersive X-ray Fluorescence (EDXRF) analysis of quartz

The chemical oxide composition of the quartz was determined using a Thermo Scientific X-ray Fluorescence (XRF) Analyser (Serial Number: 9952120). A sample size of approximately 2 g was used for analysis. Before analysis, the sample and holders were degassed for 10 min using a vacuum pump before being inserted into the XRF analyser (Aliyu et al., 2024a), (Aliyu et al., 2024b).

2.3. Scanning Electron Microscopy (SEM) of Bi ore

The microstructural properties of the Bi ore were examined using Variable Pressure Scanning Electron Microscopy (VPSEM, Model: JEOL JSM IT-300 LV, Japan) instrument. Before imaging, the samples were prepared by spray-coating onto epoxy tape to ensure adequate coverage. The samples were then degassed and imaged under vacuum at a magnification of × 1000, following the procedure reported in the literature (Aliyu et al., 2024c).

2.4. Energy Dispersive X-ray (EDX) of Bi ore

The EDX analysis of the Bi ore sample was conducted using the mapping technique using the JEOL VP-SEM analyser. The mapping feature of the VP-SEM software was used to determine the elemental composition of metals and non-metals in each sample, based on EDX

Fig. 1. (a) Glass sand and (b) powdered glass sand.

Fig. 2. Bismuth ore sample.

peak size and charge balance, by mapping out specific zones of interest on the SEM micrographs (Aliyu et al., 2024c).

2.5. Glass fabrication and characterisation

2.5.1. Glass fabrication

A series of glasses with the chemical formula {85 [25 (Quartz) + $35H_3BO_3$ + $40Na_2CO_3$] + 15BaO}(100-y) + [Bismuth ore]y, where y ranges from 5 to 25 wt%, was fabricated using the melt-quenching method. Powdered quartz was used as the primary glass former. The samples were weighed according to their proportions in the empirical chemical formulas using an electronic balance (Model: Adam PW 184; Serial number 180 AE437713). The weighed chemicals were then mixed and stirred for about 30 min in a clean alumina crucible to achieve a homogeneous mixture (Aliyu et al., 2024a) (Shaari et al., 2022). The mixture was preheated at 400 °C for 1 h to remove moisture due to the hygroscopic nature of H_3BO_3 (Umar et al., 2017). It was then immediately transferred to another furnace for melting at 930 °C for 2 h. The molten glass was cast into a preheated mould and subsequently annealed at 450 °C for 1 h to relieve thermal stress and eliminate bubbles (Tafida et al., 2020), (Alazoumi et al., 2018). The thickness of the fabricated glasses was measured using a digital vernier calliper. Finally, the glasses were polished to a mirror finish using silicon carbide paper with a smooth surface. The glass fabrication process is illustrated in Fig. 3(a–c).

2.5.2. Measurement of mass density

The mass density of each glass sample was measured directly using a calibrated automatic densitometer (Model: MH-300A; Serial No: 50.20234090012) (Aliyu et al., 2024a), based on Eq. (1).

Fig. 3. Glass fabrication process (a) Digital Weighing Balance (b) Preheating Muffle furnace (c) Melting Muffle furnace.

$$\rho_{sample} = \frac{W_{air}}{W_{water}} \rho_{water} \quad (1)$$

Where ρ_{sample}, ρ_{water}, W_{air}, W_{water} represent sample density, density of distilled water, and weight of sample in air/distilled water, respectively.

2.5.3. Optical characterisation

The optical absorption spectra of the polished glass samples were recorded at room temperature using a UV–visible spectrophotometer (Model: Jenway 741501; Serial No. 77437) over the spectral range of 400 nm–800 nm.

2.5.4. XRD analysis of the glass

The XRD characterisation of the glass samples was conducted using an X-ray diffractometer (Model: Thermo Scientific ARL'XTRA; Serial No. 197492086). Powdered glass samples were placed on a sample holder and analysed using Cu Kα radiation (λ = 1.5406 Å) at a fixed scan speed in the 2θ range at room temperature (Aliyu et al., 2024a).

2.5.5. Fourier Transform Infrared (FTIR)spectroscopy

The FTIR spectra of the fabricated glasses were recorded using an Agilent Cary 630 FTIR spectrometer equipped with an attenuated total reflectance (ATR) device, over the spectral range of 4000 cm^{-1} - 600 cm^{-1} (Aliyu et al., 2024a).

2.5.6. X-ray attenuation experiments

X-ray shielding experiments were conducted using a digital mobile X-ray machine (Model: Siemens Polymobil 2; Serial No: 02441502), following established procedures in the literature (Aliyu et al., 2024a), (Kaewjaeng et al., 2020). The setup, illustrated in Fig. 4, consisted of a glass holder positioned 40 cm from the X-ray tube and a detector probe placed 100 cm away. The X-ray beams were collimated to 1 cm × 1 cm. Attenuation experiments were performed at tube voltages of 40, 50, 60, 70, and 80 keV, with a constant current of 20 mAs. Dose rates (in μSv/hr) were recorded using a calibrated dosimeter (Model: GCA-07W; Serial No: 10325) equipped with a neon halogen tube and 0.38-inch mica window (Aliyu et al., 2024a).

2.5.7. Gamma attenuation experiment

The geometry for the point gamma-ray attenuation experiment was determined according to the method reported in the literature (Shaari et al., 2022). The specifications of the point Cs-137 source and the instruments used are presented in Tables 1 and 2, respectively.

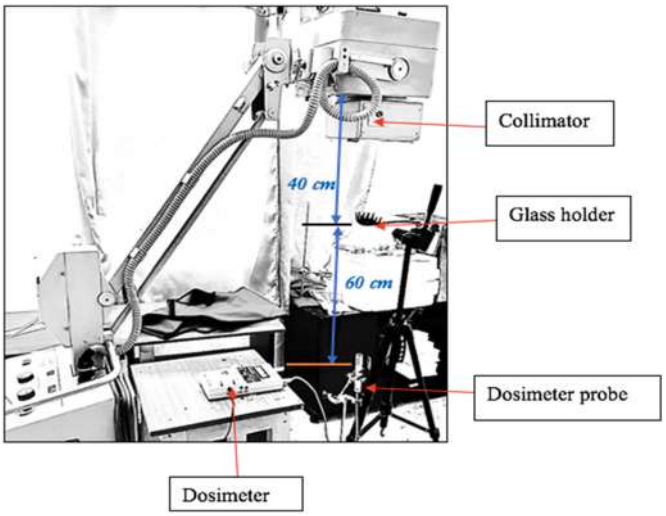

Fig. 4. Set-up for X-ray attenuation experiment (Singh et al., 2014).

Table 1
Gamma source specification.

Radionuclide	Energy (keV)	Half-life (years)	Initial Activity (A0)	Date of Manufacture
Caesium-137	661.7	30.14	1110 MBq	November 6, 2000

Table 2
Instrument specifications.

Gamma source	Caesium-137 (Cs-137)
Type of detector	RADOS Survey Meter (RDS-120) which gives a dose rate (0.05 μSv/hr – 10 Sv/hr) NaI (Tl) scintillation detector (Ludlum Survey Meter Model 44–10) which gives count rate in units of counts/min (C/m)
Source-to-detector distance	32 cm
Collimator	Lead blocks collimation
Measurement time	60 s

3. Results and discussions

3.1. Results of EDXRF analysis of glass sand

Table 3 presents the EDXRF results of the silica sand analysed in this study. The quartz (silica sand) contains 89.74 % silica, with other metallic oxides present in trace amounts. This percentage purity falls within the range reported for silica sand deposits in Nigeria, which varies from 81.5 % in Zauma River, Zamfara State (Sani et al., 2013), to 96 % in Ebenebe, southeastern Nigeria (Ene et al., 2018).

3.2. Results of EDX mapping of Bi ore

Table 4 shows the EDX results for the Bi ore, which contains elements such as C, O, V, Cu, Al, and Si in varying concentrations. However, vanadium (V) was not detected when the scanning wavelength was increased to 25 μm and 50 μm (Fig. 5). The elemental composition of Bi in the sample was 60.68 wt%. SEM analysis revealed a uniform distribution of dispersed particles in the powdered Bi ore, with variable shapes and amorphous morphology. The Bi content varied with scanning wavelength, from 58.60 wt% at 5 μm to 62.90 wt% at 25 μm and 60.6 wt% at 50 μm. The SEM micrographs (Fig. 5a–c) showed evenly distributed particles with aggregations, indicating mineral heterogeneity. The characterized Bi ore and silica sand were subsequently used to fabricate glass series.

3.3. Result of glass fabrication

Fig. 6 showcases the fabricated glasses with varying concentrations of Bi_2O_3 ore (y = wt.% of Bi), exhibiting a range of distinct colours. The glasses were transparent and bubble-free, indicating successful fabrication. The addition of Bi ore, with BaO content held constant, resulted in a

Table 3
Results of EDXRF analysis of silica sand.

Metal oxides	Normalised concentration (%)
SiO_2	89.738
Al_2O_3	5.483
MgO	1.648
K_2O	0.766
Fe_2O_3	0.698
BaO	0.538
SrO	0.418
P_2O_5	0.313
Bi_2O_3	0.256
Nb_2O_5	0.142

Table 4
Results of EDX mapping for bismuth ore.

Element	Weight %	Atomic %
C	18.94	52.25
O	17.39	35.94
Al	0.32	0.4
V	5.57	3.65
Si	0.23	0.82
Cu	0.58	0.30
Bi	60.68	9.62

progression of yellow hues specifically, three faint yellow and two yellow colours. This colouration is consistent with previous research, which attributes the yellow colour to the reduction of Bi during high-temperature melting (>900 °C). This correlation highlights the significant impact of Bi_2O_3-containing ore on the physical properties of the glass, particularly its optical characteristics.

3.4. Results measurement of density of the glasses

Fig. 7 illustrates the variation in glass density with increasing Bi ore content. The densities of the glass samples increased from 2.92 gcm^{-3} to 3.53 gcm^{-3} as the dopant content rose from 5 to 25 wt%. While for $Y = 10, 15, and\ 20$ the densities were 3.03 gcm^{-3}, 3.18 gcm^{-3} and 3.39 gcm^{-3}, respectively. This increase can be attributed to the high atomic number of Bi, as well as the presence of other heavy metal oxides in the bismuth ore, such as CuO, Al_2O_3 and V_2O_5 oxides, which may have contributed to the enhanced density and thus radiation shielding of the glasses. The study confirms that the addition of Bi ore to the glass matrix increases its density, thereby improving its radiation attenuation properties (Geidam et al., 2022a), (Amat, 2018a), (Halimah et al., 2019).

3.5. Results of optical characterisation of the glasses

3.5.1. Optical band gap

The optical band gap energy was calculated using the Mott and Davis relation [Eq. (2)], which relates the vibration frequency to the optical band gap energy (E_{opt}) as follows:

$$\alpha\hbar\omega = B\left(\hbar\omega - E_{opt}\right)^n \tag{2}$$

Where ∝ is the coefficient of absorption, $\hbar$: is the reduced Planck constant (Dirac constant) and B: is a constant. For the indirect transitions, $n = 2$, while for direct transitions $n = ½$. The optical data was analysed for higher values of $(\hbar\omega)$ above the exponential region by plotting $(\alpha\hbar\omega)^{½}$, as a function of (ħω). The respective values of E_{opt} obtained when extrapolating the linear parts of the curves to $(\alpha\hbar\omega)^{½} = 0$ for an indirect transition and $(\alpha\hbar\omega)^2 = 0$ for a direct transition. Using the Mott-Davis equation, a plot of $(\alpha\hbar\omega)^2$ versus $(\hbar\omega)$ (Ab Rasid et al., 2014), (Amat, 2018a), (Aliyu et al., 2024b).

3.5.2. Refractive index

The refractive indices, n, of the glass samples, were evaluated from the optical band gap values using Eq. (3) proposed in the literature (Dimitrov and Sakka, 1996).

$$\frac{(n^2-1)}{(n^2+2)} = 1 - \sqrt{\frac{E_{opt}}{20}} \tag{3}$$

As shown in Table 5, the refractive indices of the glasses generally increased with rising Bi2O3 content, except for glass Y10, which exhibited a skewed refractive index likely due to its higher Urbach energy. The increase in refractive index with Bi_2O_3 content can be attributed to the large atomic weight of bismuth (Aliyu et al., 2024b). However, the anomalous behaviour of glass Y10 may be linked to the use of ore-based Bi oxide, which potentially introduces other metals that influence its optical properties, leading to the observed deviation in refractive index. This skewness may have implications for the application of glasses made with bismuth ores in laser and optoelectronic devices, where precise control over the refractive index is crucial for optimal performance. The variability in refractive index could affect the glasses' suitability for such applications, highlighting the need for careful consideration of ore composition and processing conditions (Aliyu et al., 2024a), (Lamarsh, 1967).

The *Urbach* energy, ΔE (Eq. (4)), is the degree of defects and disorderliness in a material. The higher values of *Urbach* energy seen in Y10 glass indicate a higher probability of transforming weak bonds into defects (Aliyu et al., 2024b).

$$\alpha(\omega) = Be^{\hbar\omega/\Delta E} \tag{4}$$

The term B is a constant, $\hbar\omega$ is the photon energy and $\alpha(\omega)$ is the absorption coefficient. From Table 5, the increased Urbach energy in Y10, Y15, and Y20 shows rising defects in the glass systems and more chances to convert weak bonds into defects (Aliyu et al., 2024a), (Mohd Fudzi et al., 2017).

Fig. 8 illustrates the variation of indirect band gap energy with Bi ore content in glasses Y5 to Y25 (samples GLS5 to GLS25). The indirect band gap values, obtained from Tauc plot, range from 1.54 eV to 2.24 eV as the Bi ore content increases from 5 % to 25 %. However, the trend is non-monotonic, with the highest band gap (2.24 eV) observed at 5 % Bi, while the lowest (1.54 eV) is at 10 % Bi. This irregular trend is consistent with previous reports on similar glass systems [(Amat, 2018b). The changes in band gap can be attributed to the role of Bi^{3+} ions in modifying the glass network, potentially creating more bridging oxygen sites and strengthening covalent bonds (Hamza et al., 2019a). The variation in band gap energy with Bi ore content is due to the formation of bridging oxygens (BOs) and non-bridging oxygens (NBOs) in the glass network. The increase in band gap at certain Bi ore concentrations is linked to the creation of BOs, while the decrease at other concentrations is associated with the formation of BO_3 and NBOs. The NBOs reduce the energy gap by creating localized states, making it easier for electrons to transition from the valence band to the conduction band (Thakur et al., 2023), (Hamza et al., 2019b). Comparison with other glass systems reported in the literature (Hamza et al., 2019a), (Krishna Reddy et al., 2019), (Fudzi et al., 2017) reveal that the band gap values of the present glasses are generally lower, potentially due to differences in dopant concentration or the fact that ores and not analytical grade chemicals were used. The implications of these results are significant for applications in optoelectronics and radiation shielding, where precise control over optical properties is crucial.

Fig. 9 presents the Urbach Energy of Glass samples Y5 to Y25. The Urbach energy (EUr) values, which range from 0.38 eV to 1.58 eV, show non-linear behaviour. The increase in EUr with dopant addition suggests an increase in defects, potentially leading to weak bonds and instability in the glass system (Aliyu et al., 2024b), (Han et al., 2021), (Aliyu et al., 2024d). The high EUr values (1.59 eV, 1.42 eV, and 1.08 eV) in some samples indicate that these glasses do not fit the category of vitreous semiconducting glasses, which typically have EUr values between 0.66 eV to 0.045 eV (Davis and Mott, 1970). Instead, the EUr values agree with those reported for glasses with similar compositions, such as 0.686 to 1.171 eV (Azlan et al., 2019) and 1.15 to 1.82 eV (Aliyu et al., 2024d). Glasses with EUr values between 0.32 and 0.58 eV, 0.37 and 0.63 eV, and 0.235 and 0.272 eV have been reported for vitreous semiconducting glasses (Kundu et al., 2014), (Dalal et al., 2015). The implications of these results are significant for applications in optoelectronics and radiation shielding, where glass stability and defect density can impact performance. The high EUr values indicate potential limitations in these applications, highlighting the need for careful control over glass composition and processing conditions.

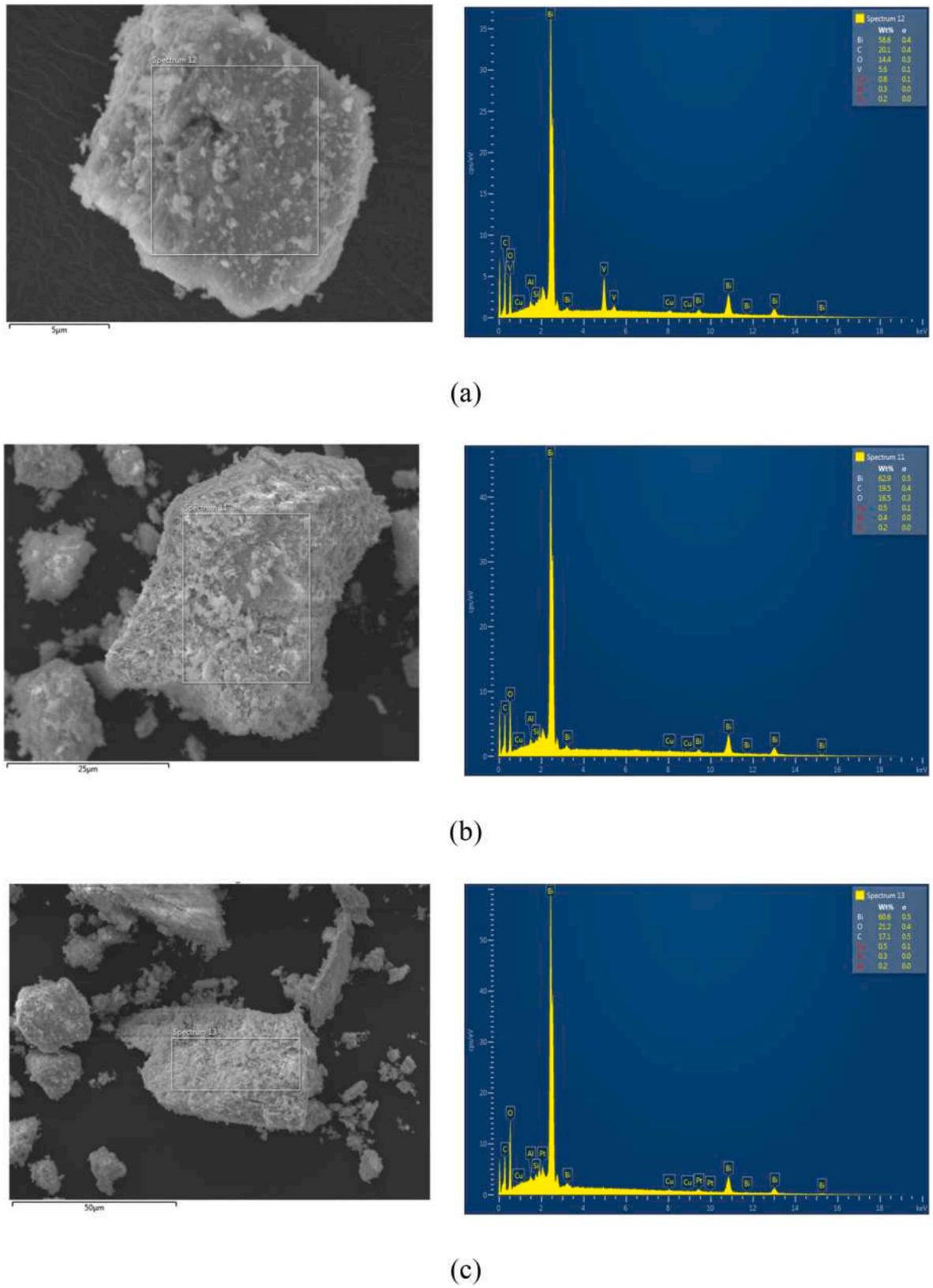

Fig. 5. SEM Micrographs and Spectrum of Bi for exposure at (a) 5 µm, (b) 25 µm (c) 50 µm.

3.6. Results of XRD and FTIR analyses of glass samples

Fig. 10 presents the XRD spectra of the fabricated glass samples, which exhibit characteristic amorphous patterns. The absence of sharp peaks and the presence of a broad hump between 20° and 35° confirm the amorphous nature of the samples, indicating no crystalline phases are present (Azlina et al., 2024), (Azlan et al., 2019) (Alazoumi et al., 2018), Fig. 12 presents the FTIR spectra of silica sand co-doped with

Fig. 6. Fabricated Glasses with Y = wt.% Bi_2O_3 Ore in the glass series.

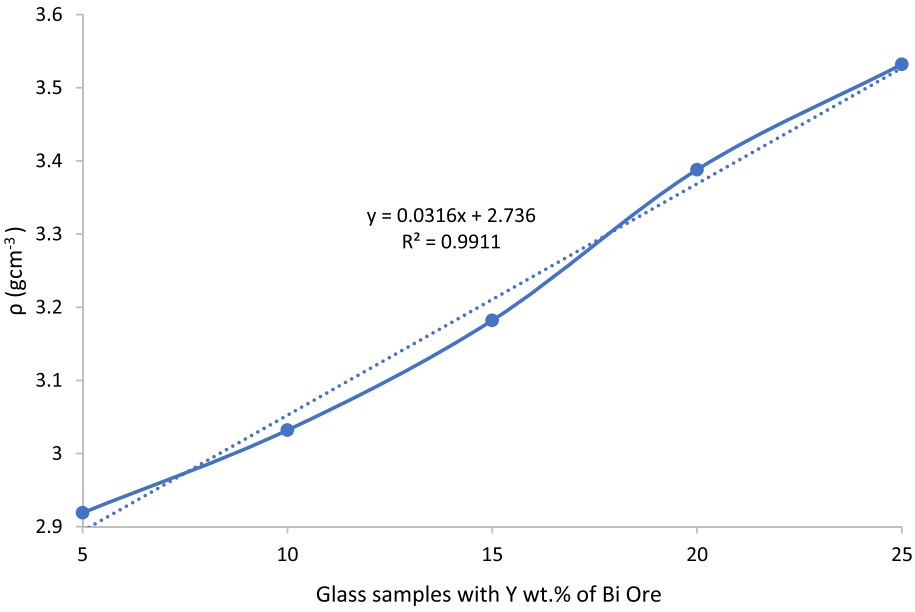

Fig. 7. Variation of Density of Glass Samples with increasing Bismuth ore (wt.%).

Table 5
Optical bandgap, refractive index and Urbach energy.

Bismutite Y (wt. %)	Band Gap Energy (eV)	Refractive Index (n)	Urbach Energy
5	2.24	2.24	0.38
10	1.54	2.49	1.59
15	1.98	2.31	1.42
20	1.95	2.32	1.08
25	1.90	2.34	0.60

bismuth ore and barium oxide glass samples in the range of 4000 to 600 cm^{-1}, exhibiting various stretching, bending, and vibrational bands that provide insight into the local structure of the glasses. The spectra reveal key absorption bands, including symmetric stretching vibrations of Bi–O bonds in BiO3 pyramidal units (872-1200 cm^{-1}) (Geidam et al., 2021), Bi–O–Bi vibrations of BiO6 structural units (1222 cm^{-1}) (Almuqrin and Sayyed, 2021). B–O stretching in BO3 ufig11nits (1408 cm^{-1}) (Hamza et al., 2019c), B–O stretching vibrations of BO4 units (1013 cm^{-1}) (Geidam et al., 2022b), (Thakur et al., 2023) and stretching modes of Si–OH (1751 cm^{-1}) (Krishna Reddy et al., 2019) and OH- group (2870 cm^{-1}) (Geidam, 2022) (see Fig. 11).

3.7. Result of nuclear radiation attenuation experiments

3.7.1. Results of X-ray attenuation experiment

The linear attenuation coefficient (LAC), determined from measured dose rates before and after glass insertion, follows the Lambert relations for photon attenuation as described in Eq. (5). LAC quantifies the probability of photon interaction per unit path length in the absorber, providing insight into the radiation shielding effectiveness of the material (Aliyu et al., 2024a), (Aliyu et al., 2024e).

$$ln\left(\frac{I}{I_o}\right) = \mu x \tag{5}$$

Where μ is LAC measured in cm^{-1}. As seen in Fig. 9, the LAC of the glass system decreases with increasing X-ray tube voltage. This affirms the

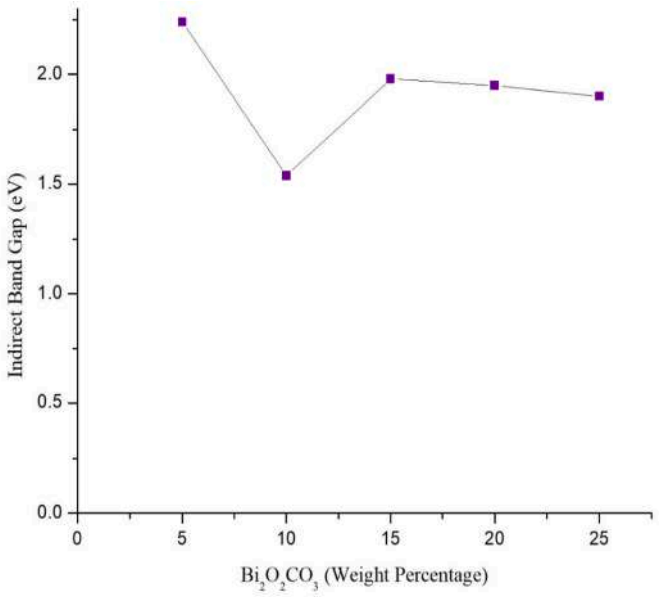

Fig. 8. Variation of Indirect Band Gap of the synthesized glasses against weight percentage.

direct and inverse relationship with the cross-section of the photoelectric effect on atomic number and photon energy, respectively (Aliyu et al., 2024a) as seen in Eq. (6), (L'Annunziata, 2003):

$$\sigma_{PE} = \frac{Z^5}{(h\nu)^{\frac{7}{2}}} \tag{6}$$

The photoelectric effect cross-section (σ_{PE}) is directly related to the atomic number (Z) and increases with the Bi oxide content, resulting in a higher effective atomic number of the glass system (Aliyu et al., 2024a). Conversely, as the X-ray energy increases, σ_{PE} decreases, leading to a corresponding decrease in the linear attenuation coefficient (LAC), as evident in Fig. 12, where the photon energy (hv) plays a crucial role in determining the interaction probability (Aliyu et al., 2024a). As the X-ray energy increases, the photoelectric effect cross-section decreases, resulting in lower linear attenuation coefficients (LACs), as shown in Fig. 13 (Aliyu et al., 2024a), (Das and Ferbel, 2003). The LACs of all glass samples decrease with increasing photon energy (40–80 keV), with Y20 glass exhibiting the highest LAC at most energies and Y25 at 40 keV. Conversely, the glass with 10 % Bi ore has the lowest LAC at higher energies (70 and 80 keV). For tube voltages above 40 keV, the glass sample with 25 wt% dopant exhibits the highest linear attenuation coefficient (LAC) values, whereas the sample with 5 wt% dopant has the lowest LAC at tube voltages ≤60 keV. Notably, at 70–80 keV, the increased Bi^{3+} concentration in the 25 wt% doped glass leads to a K-edge effect, resulting in a sudden increase in photoelectric absorption and a corresponding rise in LAC.

Fig. 13 shows the mass attenuation coefficients (MACs) of the fabricated glasses, with the glass containing 20 % Bi ore exhibiting higher MAC values across all tube voltages. The methodology for calculating X-ray shielding parameters using the experimental geometry is detailed in the literature (Aliyu et al., 2024e). Key parameters for evaluating X-ray shielding effectiveness include the half-value layer (HVL), tenth-value layer (TVL), and mean-free path (MFP), with lower HVL and MFP values indicating better shielding materials [71]. HVL, defined as the thickness required to reduce the transmitted intensity to 50 % of the initial intensity, is a crucial metric for determining the effectiveness of X-ray or gamma-ray shielding, as given by Eq. (7).

$$HVL = \frac{In(2)}{\mu} \tag{7}$$

The half-value layer (HVL) is calculated using the linear attenuation coefficient (μ) as per Eq. (7). Fig. 14 shows that the glass sample with 15 % dopant has higher HVL values at most tube voltages, except at 70 keV and 80 keV, where the 10 % dopant glass exhibits higher HVL. In contrast, glasses with 20 % and 25 % dopant have comparable HVL values at tube voltages ≤60 keV. Notably, the 20 % doped glass outperforms the 25 % doped glass at higher voltages (70 and 80 keV) due to its lower HVL values. Moreover, the 20 % doped glass surpasses

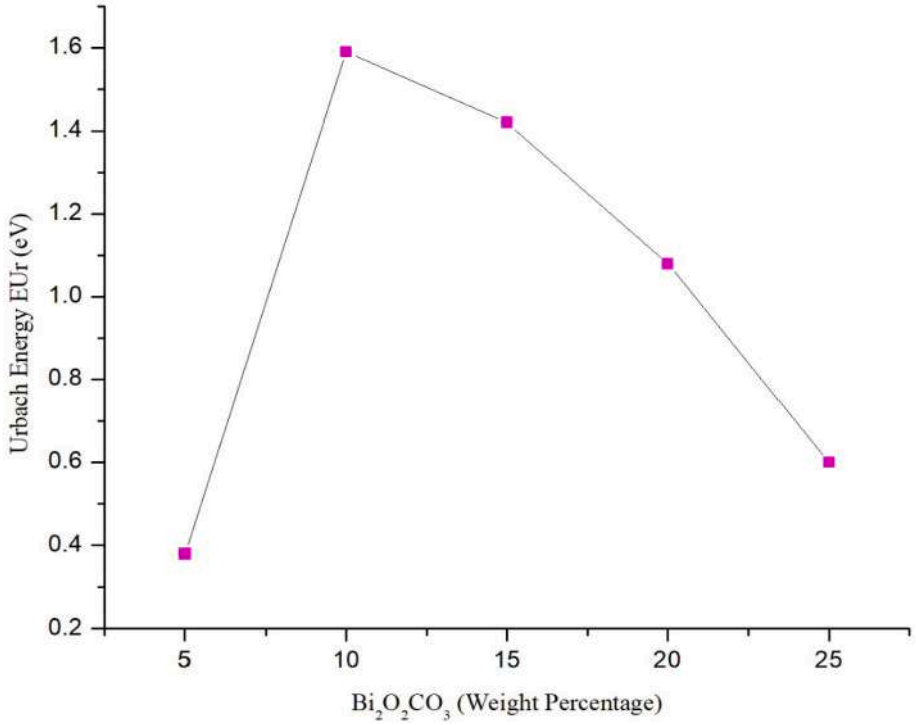

Fig. 9. Variation of Urbach Energy of the Synthesized Glasses against Weight Percentage of Bismuth ore (Bismutite) $Bi_2(CO_3)O_2$.

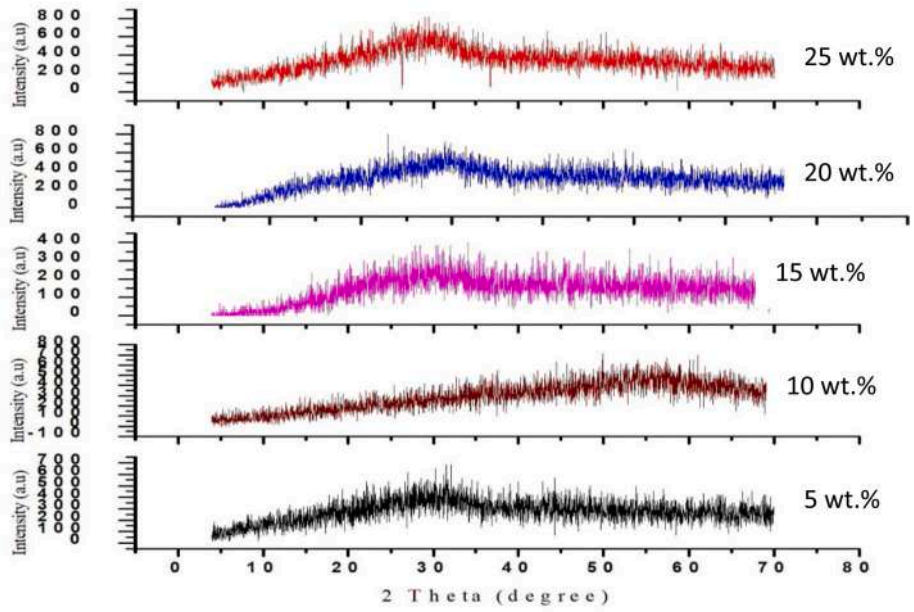

Fig. 10. XRD spectra of the fabricated glass samples showing the wt.% of bismuth ore in each samples.

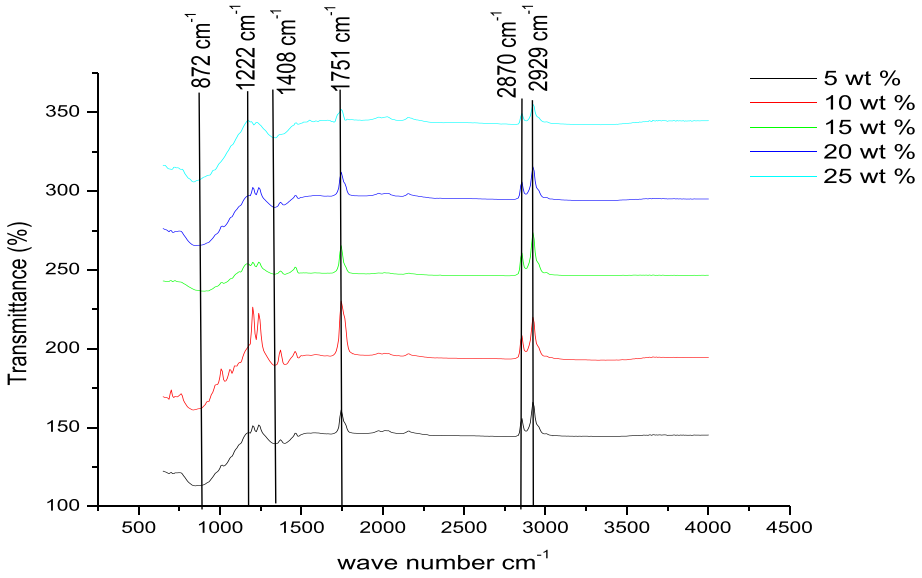

Fig. 11. FTIR Spectra for the glass system.

commercial Pb/Ba glass at both low and high tube voltages, demonstrating its potential as a competitive and innovative material for low-energy X-ray attenuation.

Fig. 15 shows that Y20 glass has the lowest TVL across various tube voltages, followed by Y25, while Y10 has the highest TVL at 80 keV. This indicates that Y20 is the most efficient at attenuating high-energy photons. Additionally, Fig. 16 compares the MFP of the fabricated glasses to commercial Pb/Ba glass. The results reveal that the glass with 20 % dopant has the shortest MFP across all photon energies due to the increased disorderliness in the glass network promoted by the higher Bi content.

3.7.2. *Results of gamma-ray attenuation experiment*

Table 6 shows that glass Y25, with the highest Bi_2O_3 content, exhibits the lowest TVL and MFP values, indicating enhanced gamma-ray attenuation (662 keV) with increasing Bi ore content. Notably, the new glass system outperforms commercial Pb/Ba glass used in local hospitals (Fig. 17). Interestingly, the results also suggest that higher defects (*Urbach* energy) in glass Y10 do not translate to improved gamma or X-ray attenuation efficiency, highlighting the importance of Bi content in determining shielding performance.

4. Conclusion

This study successfully fabricated a novel glass series with the composition {85 [25 (Quartz) + $35H_3BO_3$ + $40Na_2CO_3$] + 15BaO}(100-y) + [Bismuth ore]y ($5 \leq y \geq 25$ wt%), utilizing characterized glass sand, co-doped Bi oxide ore, and analytical-grade Ba oxide. The resulting glasses exhibited high transparency and a linear increase in density with rising Bi oxide ore concentrations. The findings can be attributed to the high atomic mass and density of Bi oxide and Ba oxide modifiers, which enhance the photon-matter interaction and subsequent radiation attenuation. XRD analysis confirmed the amorphous nature of the glasses, despite using crude metal oxides, indicating a disordered glass

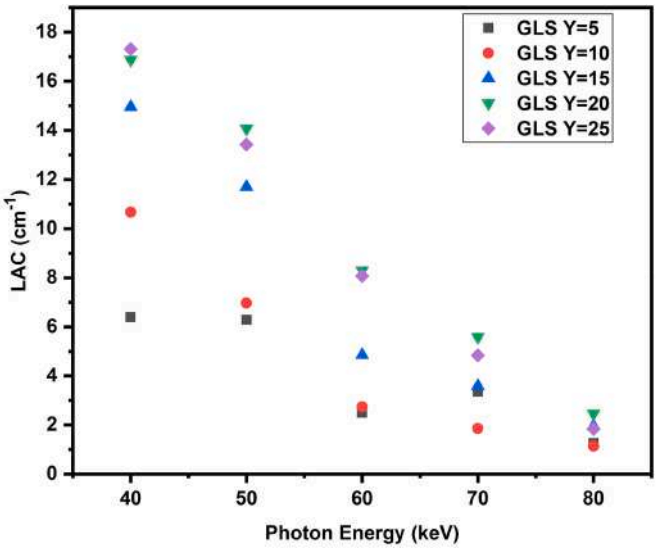

Fig. 12. Linear Attenuation Coefficient of fabricated glass systems.

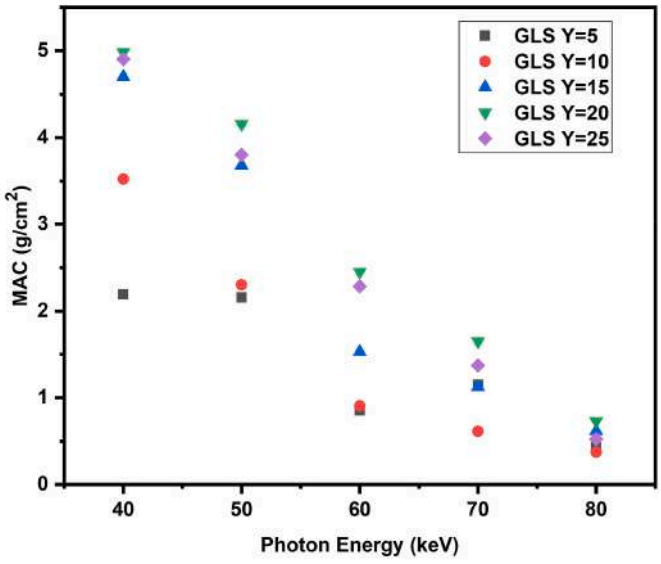

Fig. 13. Mass Attenuation Coefficient of the fabricated glass.

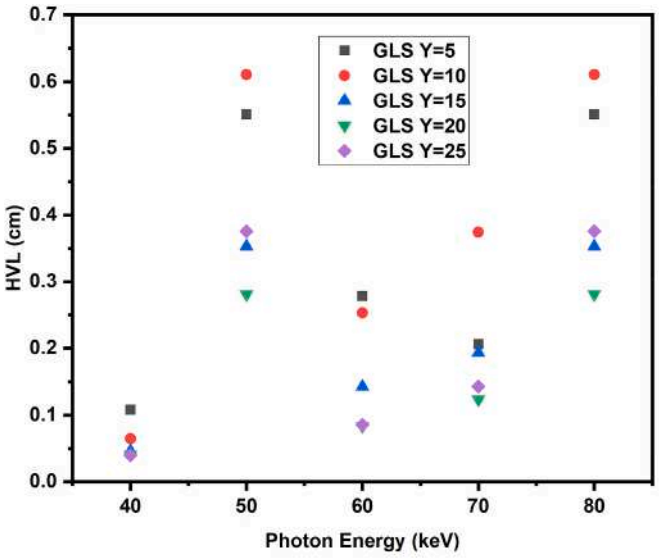

Fig. 14. Half Value Layer of glass systems compared to commercial Pb/Ba glass.

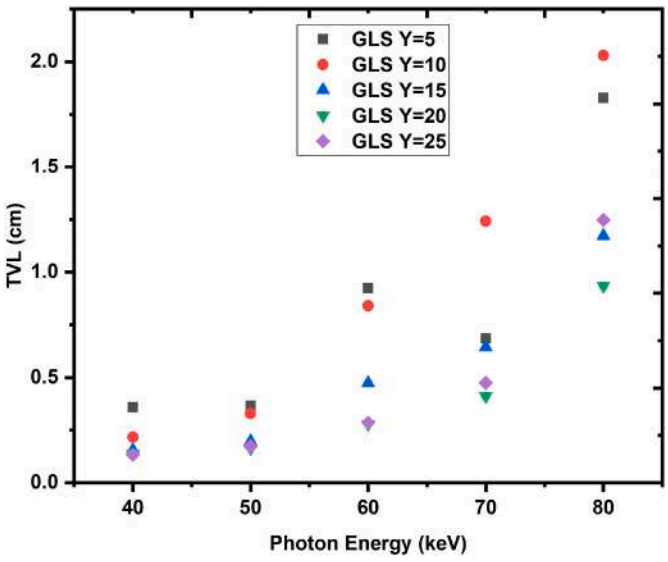

Fig. 15. Tenth Value Layer of fabricated glass systems.

network that promotes photon scattering and absorption. Notably, the glasses demonstrated promising X- and gamma-ray shielding efficiency, with the Y20 glass sample exhibiting optimal performance, outperforming commercial Pb/Ba glass in terms of lower HVL and MFP values. The enhanced shielding efficiency can be attributed to the increased Bi content, which promotes disorderliness in the glass network, resulting in enhanced photon attenuation via photoelectric absorption for X-rays and Compton scattering for gamma rays, where the latter exhibits two orders of magnitude higher photon intensity. The cost-effectiveness and environmental benefits of using Bi oxide ore and glass sand as raw materials make these glasses an attractive alternative to traditional radiation shielding materials. These findings suggest that the developed glasses have potential applications in medical facilities, nuclear power plants, and other industries requiring radiation protection, where the glasses' unique properties can be leveraged to reduce radiation exposure and improve safety. The results of this study significantly enhance the current understanding of radiation shielding materials, shedding new light on the design and development of more effective, sustainable, and affordable radiation shielding solutions. Overall, this study contributes to the development of radiation shielding materials with significant implications for future research, warranting further investigation into the optoelectronic properties of these glasses and optimization of glass formulations for specific applications, such as space exploration and nuclear medicine.

CRediT authorship contribution statement

Abubakar Sadiq Aliyu: Writing – review & editing, Project administration, Investigation, Funding acquisition, Formal analysis, Data curation, Conceptualization. **Sulaiman Yaro Jibrin:** Writing – original draft, Methodology, Formal analysis, Data curation, Conceptualization. **Amina Muhammad Dunama:** Methodology, Investigation, Data curation. **Umar Sa'ad Aliyu:** Methodology, Funding acquisition, Formal analysis, Conceptualization. **Abdulkarim Muhammad Hamza:** Writing – review & editing, Validation, Supervision, Funding acquisition, Conceptualization. **Bemgba Bevan Nyakuma:** Writing – review & editing, Validation, Resources, Investigation. **Jamilu Ari Labaran:**

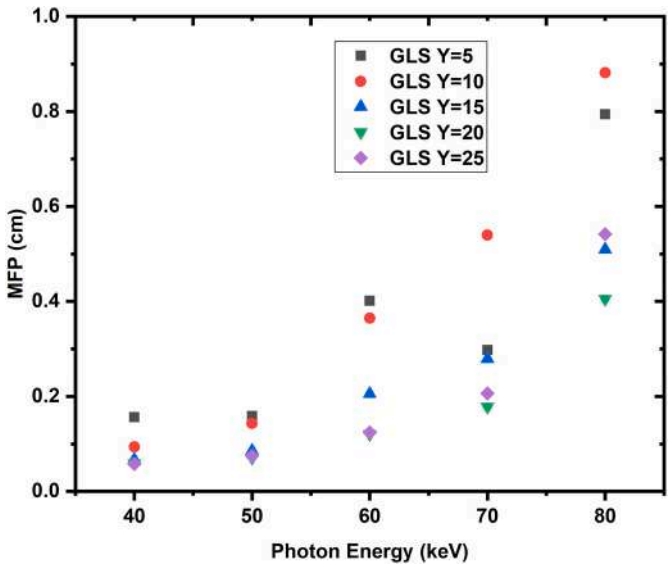

Fig. 16. Mean Free Path of the glass system.

Table 6
Gamma attenuation parameters for Cs-137 source.

Y (wt.%)	*LAC* (cm^{-1})	MAC (gcm^{-2})	HVL (cm)	TVL	MFP
5	0.20	0.07	3.50	11.61	5.04
10	0.20	0.07	3.50	11.61	5.04
15	0.12	0.04	5.99	19.90	8.64
20	0.25	0.07	2.81	9.35	4.06
25	0.27	0.08	2.58	8.58	3.73
Commercial	0.11	0.02	6.32	21.00	9.12

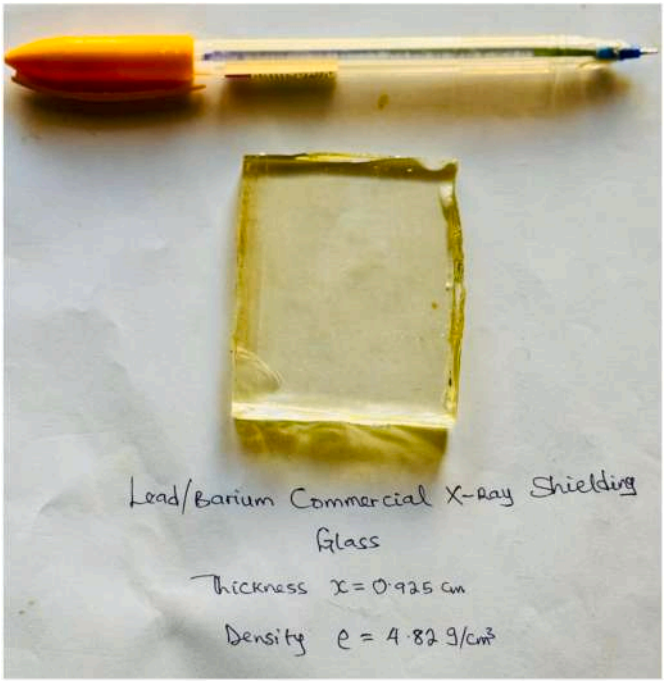

Fig. 17. Commercial lead/barium X-rays shielding glass.

Writing – review & editing. **Yahaya Musa:** Validation, Methodology. **Abdulsamad Asuku:** Visualization, Validation, Methodology. **Sani Muhammad:** Software, Visualization.

Ethical approval

Not applicable to the current study.

Availability of data and materials

All data related to the paper are presented in the text.

Funding

This research was partly funded by theTertiary Education Trust Fund (TETFund) of the Federal Republic of Nigeria under the National Research Fund 2021 (Project Code: TETFES/DR&-CE/NRF-2021/SETI/SAR/00031/VOL.1).

Declaration of competing interest

The authors declare that they have no known competing financial interests or personal relationships that could have appeared to influence the work reported in this paper.

Data availability

Data will be made available on request.

References

Ab Rasid, A., Wagiran, H., Hashim, S., Hussin, R., Ibrahim, Z., 2014. Optical properties of undoped and Dy3+-doped boro-tellurite glass. Adv. Mater. Res. 194–199. https://doi.org/10.4028/www.scientific.net/AMR.895.194.

Aboud, H., Mkhaiber, A.F., Alajermi, Y., 2022. Radiation shielding properties of Cd-Bi-Pb-Zn-borate glasses: influence of Bi2O3 activation. Phys. Scri. 97 (11), 114001. https://doi.org/10.1088/1402-4896/ac6af0.

Al-Buriahi, M.S., et al., 2021. Role of heavy metal oxides on the radiation attenuation properties of newly developed TBBE-X glasses by computational methods. Phys. Scri. 96 (7). https://doi.org/10.1088/1402-4896/abf86a, 0–15.

Alazoumi, S.H., et al., 2018. Optical properties of zinc lead tellurite glasses. Results Phys. 9 (March), 1371–1376. https://doi.org/10.1016/j.rinp.2018.04.041.

Aliyu, A.S., et al., 2024a. Bismuthite and cassiterite-doped borosilicate glass systems for X-rays attenuation: fabrication and characterisation. Opt. Mater. 151 (April), 115365. https://doi.org/10.1016/j.optmat.2024.115365.

Aliyu, A.S., et al., 2024b. Optoelectronic and gamma ray attenuation properties of ore-based Bi and Sn-doped borosilicate glasses. Ceram. Int. 50 (15), 26424–26434. https://doi.org/10.1016/j.ceramint.2024.04.369.

Aliyu, A.S., et al., 2024c. Synthesis and characterisation of rice husk and palm fruit bunch silica: compositional, structural, and thermal analyses. Biomass Convers. Biorefin. https://doi.org/10.1007/s13399-024-05525-1.

Aliyu, A.S., et al., 2024d. J. Ceram. Int. https://doi.org/10.1016/j.ceramint.2024.04.369.

Aliyu, A.S., et al., 2024e. Physical, structural and X-rays attenuation properties of bismuthite and cassiterite-doped borosilicate glass systems. Opt. Mater. (in press).

Almisned, G., et al., 2021. Gamma, fast neutron, proton, and alpha shielding properties of borate glasses: a closer look on lead (II) oxide and bismuth (III) oxide reinforcement. Appl. Sci. (Switzerland) 11 (15). https://doi.org/10.3390/app11156837.

Almuqrin, A.H., Sayyed, M.I., 2021. Radiation shielding characterizations and investigation of TeO2–WO3–Bi2O3 and TeO2–WO3–PbO glasses. Appl. Phys. A Mater. Sci. Process. 127 (3), 1–11. https://doi.org/10.1007/s00339-021-04344-9.

Alonizan, N., et al., 2023a. Physical, optical, and ionizing radiation shielding properties for barium–tellurite glass with different oxides: an experimental study. Opt. Mater. 143, 114177. https://doi.org/10.1016/j.optmat.2023.114177.

Alonizan, N., et al., 2023b. Mechanical, structural, and radiation shielding characteristics for transparent boro-tellurite glasses modified with strontium and bismuth oxide ratios. Opt. Mater. 146, 114524. https://doi.org/10.1016/j.optmat.2023.114524.

Aloraini, D.A., Almuqrin, A.H., Kaky, K.M., Sayyed, M.I., Elsafi, M., 2023. Radiation shielding capability and exposure buildup factor of cerium (IV) oxide-reinforced polyester resins. E-Polymers 23 (1). https://doi.org/10.1515/epoly-2023-0128.

Amat, A.B., 2018a. Structural, Optical and Gamma Radiation Shielding Properties of Bi2O3/BaO-B2o3-TeO2 Doped CeO2 Glass System. Universiti Putra Malaysia.

Amat, A.B., 2018b. Structural, optical and gamma radiation Shielding of Bi2O3/Ba2O3-TeO2 Doped with CeO2 Glass System. Universiti Putra Malaysia.

Azlan, M.N., Halimah, M.K., Suriani, A.B., Azlina, Y., Umar, S.A., El-Mallawany, R., 2019. Upconversion properties of erbium nanoparticles doped tellurite glasses for high efficient laser glass. Opt. Commun. 448 (April), 82–88. https://doi.org/10.1016/j.optcom.2019.05.022.

Azlina, Y., Shaari, H.R., Hisam, R., Al-Hada, N.M., Umar, S.A., Kenzhaliyev, B.K., 2024. Non-linear refractive index of tellurite glass doped with. AIP Conf. Proc. 1–6.

Dalal, S.R., Khasa, S., Dahiya, M.S., Yadav, A., Agarwal, A., Dahiya, S., 2015. Optical and thermal investigations on vanadyl doped zinc lithium borate glasses. J. Asian Ceram. Soc. 3, 234–239.
Das, A., Ferbel, T., 2003. Introduction to Nuclear and Particle Physics. World Scientific.
Davis, E.A., Mott, N.F., 1970. Conduction in non-crystalline systems V. Conductivity, optical absorption and photoconductivity in amorphous semiconductors. Philos. Mag. 22, 903–922.
Dimitrov, V., Sakka, S., 1996. Electronic oxide polarizability and optical basicity of simple oxides. I. J. Appl. Phys. 79 (3), 1736–1740. https://doi.org/10.1063/1.360962.
Dogra, M., Singh, K.J., Kaur, K., Anand, V., 2018. Gamma-ray shielding properties at 129·5 MBq and structural investigations of the Bi 2 O 3 –B 2 O 3 –K 2 O–Li 2 O–V 2 O 5 glass system. Eur. J. Glasses Sci. Technol. B Phys. Chem. Glasses 59 (6), 293–300. https://doi.org/10.13036/17533562.59.6.056.
El Din, H.M.N., Saeed, A., Salem, E., El Shazly, R.M., Wahab, M.A., 2024. A multi-function glass shield for neutrons and gamma rays of boron- and bismuth-reinforced silicate glass. Sci. Rep. 14 (1), 24472. https://doi.org/10.1038/s41598-024-73977-6.
Ene, E.G., Dim, C.I.P., Chidubem, E., 2018. Assessment of some pristine sand deposit from Imo Formation (southeastern Nigeria) as construction aggregate and industrial material. Environ. Earth Sci. 77 (23), 790. https://doi.org/10.1007/s12665-018-7957-6.
Fudzi, F.M., Kamari, H.M., Latif, A.A., Noorazlan, A.M., 2017. Linear Optical Properties of Zinc Borotellurite Glass Doped with Lanthanum Oxide Nanoparticles for Optoelectronic and Photonic Application, 2017.
Geidam, I.G., 2022a. Structural, Optical, Elastic and Gamma Radiation Shielding Properties of Rice Husk-Derived Silica Borotellurite Glass System Doped with Bismuth Oxide. Universiti Putra Malaysia.
Geidam, I.G., et al., 2021. Thermo-physical and elastic properties of Bi2O3 doped silica borotellurite glasses. Optik (Stuttg) 248 (2021), 12–15. https://doi.org/10.1016/j.ijleo.2021.168201.
Geidam, I.G., et al., 2022b. Oxide ion polarizabilities and gamma radiation shielding features of TeO 2 – B 2 O 3 – SiO 2 glasses containing Bi 2 O 3 using Phy-X/PSD software. Mater. Today Commun. 31 (April), 1–9.
Halimah, M.K., Azuraida, A., Ishak, M., Hasnimulyati, L., 2019. Influence of bismuth oxide on gamma radiation shielding properties of boro-tellurite glass. J. Non-Cryst. Solids 512. https://doi.org/10.1016/j.jnoncrysol.2019.03.004.
Hamza, A.M., Halimah, M.K., Muhammad, F.D., Chan, K.T., 2019a. Physical properties, ligand field and Judd-Ofelt intensity parameters of bio-silicate borotellurite glass system doped with erbium oxide. J. Lumin. 207, 497–506. https://doi.org/10.1016/j.jlumin.2018.11.038.
Hamza, A.M., et al., 2019b. Structural, optical and thermal properties of Er3+-Ag codoped bio-silicate borotellurite glass. Results Phys. 14 (June), 102457. https://doi.org/10.1016/j.rinp.2019.102457.
Hamza, A.M., et al., 2019c. Results in Physics Structural, optical and thermal properties of Er 3 + -Ag codoped bio-silicate borotellurite glass. Results Phys. 14 (March), 102457. https://doi.org/10.1016/j.rinp.2019.102457.
Han, T., et al., 2021. Role of Gd2O3 on tailoring structural and optical properties of Tb3 +-activated borogermanate-tellurite glasses. Radiat. Phys. Chem. 189, 109734. https://doi.org/10.1016/j.radphyschem.2021.109734.
Lamarsh, J.R., 1967. Introduction to Nuclear Reactor Theory. Addison-Wisely Publishing Company. New York University.
Kaewjaeng, S., Boonyu, K., Kim, H.J., Kaewkhao, J., Kothan, S., 2020. Study on radiation shielding properties of glass samples doped with holmium. AIP Conf. Proc. 2279 (1), 60005.
Karthika, S., Asokan, K., Marimuthu, K., Meena, R., Sundari, S.S., 2025. Ceramization of ABO glasses under the influence of O7+ ion irradiation. Ceram. Int. 51 (5), 6033–6047. https://doi.org/10.1016/j.ceramint.2024.12.049.
Khazaalah, T.H., et al., 2022. Development of novel transparent radiation shielding glasses by BaO doping in waste soda lime silica (SLS) glass. Sustainability (Switzerland) 14 (2), 1–11. https://doi.org/10.3390/su14020937.
Krishna Reddy, D.V., Taherunnisa, S., Lakshmi Prasanna, A., Sambasiva Rao, T., Veeraiah, N., Rami Reddy, M., 2019. Enhancement of the red emission of Eu3+ by Bi3+ sensitizers in yttrium alumino bismuth borosilicate glasses. J. Mol. Struct. 1176, 133–148. https://doi.org/10.1016/j.molstruc.2018.08.057.
Kundu, R.S., Dhankhar, S., Punia, R., Nanda, K., Kishore, N., 2014. Bismuth modified physical, structural and optical properties of mid-IR transparent zinc boro-tellurite glasses. J. Alloys Compd. 587, 66–73. https://doi.org/10.1016/j.jallcom.2013.10.141.
Li, W., Peng, M., Zhao, X., Chen, S., 2022. Properties of Bi2O3/epoxy Resin–Coated Composites for Protection against Gamma Rays. https://doi.org/10.1177/15280837211051102.
L'Annunziata, M.F., 2003. Nuclear Radiation, its Interaction with Matter and Radioisotope Decay, vol. 1. Elsevier.
Mahalingam, S., Kwon, D.S., Kang, S.G., Kim, J., 2023. Multicomponent X-ray shielding using sulfated cerium oxide and bismuth halide composites. Molecules 28 (16). https://doi.org/10.3390/molecules28166045.
Mohammed, S.A., Dachuru, R.S.R., 2024. Enhancement in the magnetic properties of yttrium orthoferrite materials by the addition of BaO–Bi2O3–B2O3 glass sintering aid. Phys. Status Solidi B 261 (2), 2300313. https://doi.org/10.1002/pssb.202300313.
Mohd Fudzi, F., Kamari, H.M., Abd Latif, A., Muhammad Noorazlan, A., 2017. Linear optical properties of zinc borotellurite glass doped with lanthanum oxide nanoparticles for optoelectronic and photonic application. J. Nanomater. 2017 (April). https://doi.org/10.1155/2017/4150802.
Nienhuis, E.T., McCloy, J.S., 2020. Low temperature sequential melting and anion retention in simplified low activity waste. MRS Adv. 5 (5), 195–206. https://doi.org/10.1557/adv.2020.52.
Ratep, A., Abdelaziem, A., Hanfi, M.Y., Mahmoud, K.A., Kashif, I., 2023. Enhancing gamma-ray shielding with bismuth oxide-infused boron oxides. Opt. Quant. Electron. 56 (2), 143. https://doi.org/10.1007/s11082-023-05788-4.
Sani, N.A., Abdulsalam, A.K., Abdullahi, U.A., 2013. Extraction and quantification of silicon from silica sand obtained from Zauma River, Zamfara state, Nigeria. Eur. Sci. J. 9 (15), 160–168.
Sayyed, M.I., Es-soufi, H., V More, C., Hanafy, T.A., 2025. Thorough analysis of bismuth-containing silicate glasses: evaluation of optical and radiation-shielding properties. Opt. Mater. 159, 116554. https://doi.org/10.1016/j.optmat.2024.116554.
Shaaban, K.S., Al-Baradi, A.M., Ali, A.M., 2022. Investigation of BaO reinforced TiO2-p2O5-li2O glasses for optical and neutron shielding applications. RSC Adv. 12 (5), 3036–3043. https://doi.org/10.1039/d2ra00171c.
Shaari, H.R., et al., 2022. Oxide ion polarizability, optical basicity, and metallization criterion of GO-coated Nd 2 O 3 (NPs) - TeO 2 glass for linear optical fibre. Chalcogenide Lett. 19 (8), 565–577.
Singh, V.P., Badiger, N.M., Kaewkhao, J., 2014. Radiation shielding competence of silicate and borate heavy metal oxide glasses: comparative study. J. Non-Cryst. Solids 404, 167–173. https://doi.org/10.1016/j.jnoncrysol.2014.08.003.
Sobolev, I.A., Lifanov, F.A., V Stefanovskii, S., Dmitriev, S.A., Zakharenko, V.N., Kobelev, A.P., 1987. Evaporation of components during the electric melting of glass. Glass Ceram. 44 (2), 51–54. https://doi.org/10.1007/BF00701102.
Sriwongsa, K., et al., 2023. The investigation optical, X/γ-Rays and neutrons shielding properties of BaO based on steel slag glass system. Integr. Ferroelectr. 238 (1), 246–261. https://doi.org/10.1080/10584587.2023.2234573.
Subedi, B., Lamichhane, T.R., 2023. Radiation shielding properties of low-density Ti-based bulk metallic glass composites: a computational study. Phys. Scri. 98 (3). https://doi.org/10.1088/1402-4896/acb623, 0–13.
Tafida, R.A., et al., 2020. Structural, optical and elastic properties of silver oxide incorporated zinc tellurite glass system doped with Sm3+ ions. Mater. Chem. Phys. 246 (February), 122801. https://doi.org/10.1016/j.matchemphys.2020.122801.
Thakur, S., et al., 2023. Thermo- and photoluminescent properties and gamma radiation shielding efficiency of NiO doped B2O3–Bi2O3 glass system. Radiat. Phys. Chem. (xx).
Turner, W., 1924. The use of boric oxide in glass-making. J. Am. Ceram. Soc. 7, 313–317. https://doi.org/10.1111/J.1151-2916.1924.TB18207.X.
Umar, S.A., Halimah, M.K., Chan, K.T., Latif, A.A., 2017. Physical, structural and optical properties of erbium doped rice husk silicate borotellurite (Er-doped RHSBT) glasses. J. Non-Cryst. Solids 472 (July), 31–38. https://doi.org/10.1016/j.jnoncrysol.2017.07.013.
Zaid, M.H.M., et al., 2021. Influence of heavy metal oxides to the mechanical and radiation shielding properties of borate and silica glass system. J. Mater. Res. Technol. 11, 1322–1330. https://doi.org/10.1016/j.jmrt.2021.01.117.